HYPERVELOCITY IMPACT MICROFOIL PERFORATIONS IN THE LEO SPACE ENVIRONMENT (LDEF, MAP AO 023 EXPERIMENT)

N92-23312

J.A.M. McDonnell
and
T.J. Stevenson
Unit for Space Sciences
Physics Laboratory
University of Kent
Canterbury, Kent UK CT2 7NR
Phone: [44] (227) 459616, Fax: [44] (227) 762616

SUMMARY

The Microabrasion Foil Experiment, comprises arrays of frames, each supporting two layers of closely spaced metallic foils and a back-stop plate. The arrays, deploying aluminium and brass foil ranging from 1.5 microns to some 30 microns were exposed for 5.78 years on NASA's Long Duration Exposure Facility (LDEF) at a mean altitude of 458 km. They were deployed on the North, South, East, West and Space pointing faces; results presented here comprise the perforation rates for each location as a function of foil thickness. Initial results refer primarily to aluminium of 5 microns thickness or greater. This penetration distribution, comprising 2,342 perforations in total, shows significantly differing characteristics for each detector face. The anisotropy confirms, incorporating the dynamics of particulate orbital mechanics, the dominance of incorporating extraterrestrial particulates penetrating thicknesses greater than 20 microns in aluminium foil, yielding fluxes compatible with hyperbolic geocentric velocities. For thinner foils, a disproportionate increase in the flux of particulates on the East, North and South faces demonstrates the presence of orbital particulates which exceed the extraterrestrial component perforation rate at 5μm foil thickness by a factor of approximately four. Although in terrestrially bound orbits, their origin has not yet been established exclusively as space debris. Sources and sinks of particulates in the LEO environment are discussed and improved relationships for conversion to impacting particle mass invoked to derive LEO and interplanetary mass distributions.

1. MICROABRASION PACKAGE (MAP) - AO 023

1.1. Introduction

Microfoil penetration techniques have been successfully employed as space particulate detectors since the beginning of space exploration. They offer high sensitivity of detection and yet are rugged and simple. Early measurements on rockets and satellites are reviewed (McDonnell, 1970) and again some 18 years later following the development of more reliable techniques and sophistication (McDonnell, 1978). The sensitivity of foil detectors is achieved by the quality of the foil and its thickness. For example at 5 microns foil thickness and for a foil defect density of 1 per 10 cm^2, optical scanning (even by the simplest of techniques such as a well adapted eye over a light table) yields an effective sensitivity of 10^{-11}g impacting particle mass (< 1 micron diameter) and a "background" flux rate of 3.10^{-5} m^{-2} sec^{-1} for 1 year of exposure. If such defects are logged or painted out before flight as in the case of LDEF MAP, reliability of detection is further improved. Combined with the identification of hypervelocity impact features by Scanning Electron Microscopy (SEM) post-flight examinations, not only can the highest confidence in a true space impact be established, but parameters of the particle such as mass or velocity can be inferred from the morphology. When, further, a second surface is placed immediately behind this foil, a *capture cell* is formed. Although *marginally* penetrating particles cannot be expected to provide ejecta which is detectable behind the foil, larger particles will penetrate and be retained even without a significant mass loss. Their matter, shocked through impact, is spread out over a cone of typically ± 30° and condenses on

the second surfaces; it is thus readily available for e.g. SEM and Energy Dispersive X-Ray (EDX) spectroscopy. With the use of a windowless detector, light elements including carbon may be studied. First results of the capture cell technique from a space deployment were reported (McDonnell et al. 1984) on NASA Shuttle flight STS-3 (Columbia). They showed, however, a flux of particles at some 10^{-11}g mass considerably lower than that inferred from the Solar Maximum Mission (SMM) surfaces (Laurance & Brownlee, 1986). More recently this SMM data has seen the benefits of the application of an improved penetration formula (McDonnell, 1991) in contrast to the initial interpretation of the craters by a formula not representative of the nature of the materials involved (e.g. Pailer & Grün, 1980).

This picture of the near Earth space environment is now being reshaped by the wide diversity and good statistics of the LDEF data over its 5.78 years exposure. Complemented by data from time-tagged events such as the IDE experiments on LDEF (Mulholland et al. , 1991) a very powerful base for the potential understanding of the properties of the flux distribution is available. Objectives of the MAP experiment can be identified.

(i) Definition of the flux distribution as a function of crater size or perforation thickness,
(ii) Determination of the 3-dimensional flux distribution,
(iii) Characterisation of the velocity distribution and angular distribution on a detector surface,
(iv) Discrimination between particle sources e.g.:
  (a) Earth-orbital or interplanetary?
  (b) if Earth-orbital, are they natural or space-debris?
  (c) if natural, are they asteroidal or cometary?
(v) Particulate chemistry.

We shall, no doubt, find that the answers reveal a mixture of sources since the mixing and comminution of matter within the solar system and the LEO environment appears to be an essential characteristic of the equilibrium distribution surrounding the Earth.

1.2. Technique and Experiment Details.

The LDEF Multiple Foil Microabrasion Package (MAP) system comprises a double layer of foils and a back-stop plate (Schematic Figure 1). The foils are bonded to meshes, in turn bonded to frames, which are bolted to a base plate occupying (for the NSEW faces) one third of an LDEF tray; the space-pointing array occupies one half tray. Figure 2 shows a sample of the spatial distribution of impacts on 5μm space-pointing aluminium foil and the effective areas of each frame.

Foils, generally comprising T6 temper rolled aluminium of 99.9% purity, range from 3.5 to 30 μm nominal thickness. Thinner foils (down to 1.5 μm of aluminium) are beaten and do contain considerable defects requiring the discrete post-flight verification of each impact site. For this reason the impacts tabulated for these foils are shown in parentheses. Rolled brass of 5μm nominal thickness was also flown to permit chemical discrimination of impactor residues from the possible presence of aluminium-rich space debris.

1.3. Exposure Configuration.

Four (double) frames were deployed on the space end, comprising top surfaces of 5μm aluminium and brass for a combination of maximum sensitivity and reliability. Eight frames of varying thickness were deployed on each of the four faces: North, South, East and West. The exposure configuration of MAP in orbit is shown in Figure 3. The offset of some 8° to 9°of the East face relative to the orbital motion vector (LDEF Newsletter May 1991) becomes significant when considering East-West flux ratios and, more especially, the North-South ratios. We shall see that it is these *ratios* that critically determine our viewpoint on whether flux particles are perhaps either orbital or interplanetary, because the access to different detector surfaces is so critically dependent upon the orientation of detectors. Figure 4 shows the MAP peripheral tray at recovery and in Figure 5 the space-pointing array (upper right).

1.4. LDEF Orbit Exposure.

The temporal mean altitude (H) of LDEF (Figure 3) over its entire exposure duration is calculated as 458 km; the total exposure time was 5.778 years (1.822×10^8 seconds). The orbital velocity at this altitude, assuming a circular orbit (LDEF's initial eccentricity e = 0.00015) is 7.64 km s^{-1} using 6371 km for the mean radius of the Earth (R_E); the escape velocity at this mean altitude is 10.81 km s^{-1}. A value of 185 km for the effective atmospheric height (h_a) is used, based on atmospheric drag calculations on a particle of 10^{-11}g, corresponding to the capture of a typical interplanetary particle within one Earth revolution. Summary exposure factors are listed in Table 1.

The effective solid angle of a flat plate parallel to the Earth's radius vector is given by $[\Delta - 0.5\sin(2\Delta)]$ steradians, where D (radians) is the angle from the nadir to the horizon (Figure 3). This corresponds to $\pi/2$ steradians effective solid angle for $\Delta = \pi/2$ radians, namely a very low orbit, and π steradians for an unshielded plate. The effective solid angle for a cone of θ radians half angle from the normal to the surface is $\pi(1 - \cos^2\theta)$ steradians. Δ is given by $\sin^{-1}(A/R)$, where $A = R_E + h_a$ and $R = R_E + H$ (Figure 3). The mean LDEF effective peripheral tray exposure solid angle (including Earth shielding) is 2.125 steradians.

Concerning exposure, we note that the radius vector of LDEF's 28.5° geocentrically inclined orbit is swept by rapid precession through a wide range of pointing directions relative to the solar ecliptic , and can perhaps in the first instance be considered "random". LDEF's orbital plane will have an average ecliptic referenced inclination of +23.5° (the polar declination) with a swing of ± 28.5°. The space-pointing end will then be exposed to interplanetary particulates over a very wide range of ecliptic latitudes throughout its orbit, namely ± 52°. This angle is further combined with the acceptance angle of a flat plate detector. We should view therefore the extraterrestrial flux on the Space end as an "average" of all ecliptic latitudes and longitudes. We also note especially that the Space and West-pointing faces have a very low probability of interception with Earth-orbital particulates. The West face cannot be impacted by orbital particulates at all unless they are on eccentric orbits and, further, only if they are near perigee when they strike LDEF. This excess velocity is required to enable them to "catch up" LDEF and though possible, the interception probability is low. The effective *penetrating* flux for the Space and West faces is further reduced due to the lower velocity of this population.

2. PERFORMANCE AND RESULTS.

2.1. Analysis Methods.

Performance of the MAP experiment, which was entirely passive in nature, was well demonstrated by the excellent condition of the aluminium and brass foils post flight. Few defects were detected due to experiment integration, launch or retrieval; in-flight exposure damage was found to be restricted to that of the experiment objective, *impact erosion*. Foil thicknesses given in Table 2 were determined by establishing the weight per unit area from samples of foil retained from the time of assembly to the meshes. An accuracy of 10μg in mass and some 1% in area measurement leads to an error of typically some 2% in thickness; this "calibration" leads to significant changes from nominal foil thicknesses. Because of the small statistical errors in the MAP flux determinations on, e.g. the East facing foils, the data is able to establish the significance of changes in the *slope* of the measured flux distribution - an indicator of perhaps the changing physics of impact or environmental changes. Scanning, performed optically in the first instance with a computer controlled 3 colour stereo television microscopy system (Paley, 1991), is followed by SEM and microanalysis using a Philips 525M microscope and PGT windowless EDS system. Hard copy colour images and digital images are available and are also archived into a database via an Ethernet network. A Sun workstation is used for feature analysis (e.g. as per Figure 6).

Results presented in this paper are restricted to foils of 5 microns or greater where the defect rate after pre-flight "painting out" is essentially zero. Sample tests on the hypervelocity characteristics of individual perforations were performed for quality control purposes, but generally the results presented here are from optical scanning without discrete impact site examination.

In scanning operations for marginal and larger (supra-marginal) holes, the area of the hole under back-lighted CCD imaging is established by pixel counting above a threshold light level. Figure 7 shows typical features. The transmitted light area is compared to a calibration curve determined by holes measured under

SEM examination. This "photometric" hole size determination is complemented by SEM analysis of the few very large perforations in a typical distribution.

MAP data - because of the multiplicity of thicknesses involved and the generally high perforation rates - is comprised of two types of data: (i) the marginal hole count (namely the number of perforations irrespective of size); this is evaluated and plotted as a function of the foil thickness at the ballistic limit f_{max}, and (ii) the perforation size distribution (hole diameter D_H) for any one value of foil, f_{max}. Marginal fluxes thus determined are shown in Table 2.

The flux distribution Φ as a function of f_{max}, $\Phi(f_{max})$, readily transforms to a particle size distribution $\Phi(d_p)$, or mass distribution $\Phi(m_p)$ of the same form because f_{max}/d_p is not a strong function of size of particle. The distribution of D_H for any value f_{max} does not, however, so transform. For the latter, the increase of hole size as a function of increasing particle size shows a rapid "onset" just above the ballistic limit; thereafter there is a convergence of the hole size D_H towards the particle diameter d_p for $d_p >> f_{max}$. Such relationships have been published by Carey et al (1985) (see Appendix) and more recently studied by Hörz et al (1991). Figures 7(a) to (c) show various hypervelocity impact features on the MAP aluminium foils ranging from marginal (at the exit side, 6(a) and (b)) and in 7(c) one which is clearly the record of a very large particle of some 30 microns diameter which continued through to deposit a spider's web of impacting particulate matter within the capture cell behind.

2.2. Marginal Flux Distributions.

The number of perforations, irrespective of size D_H, is established first for various thicknesses of foil. This yields the *cumulative* distribution $\Phi(f_{max})$ for the peripheral faces (N,S,E,W). Because only 5 microns brass and aluminium was flown on the space-pointing faces, a single value for each of the surfaces is presented. Data is shown in Figure 8 and also that from the Solar Maximum Mission Satellite (Laurance & Brownlee, 1985). We shall later use the size distribution D_H of these foils to generate an interpreted equivalent distribution (section 2.3) as a function of f_{max} e.g. Figure 9.

The marginal distribution in Figure 8 shows high definition with, generally, the exception of the West-pointing faces where counts are low. When these marginal counts are transformed to an actual size distribution, some of the coarseness of the foil thickness "quantisation" can be removed. Currently a fit through the West data is used since each point is independent.

We see an interesting divergence in the flux between the side faces of LDEF (N,S) relative to the velocity vector. As stated these (because of precession) show average exposure relative to the ecliptic elevations North and South; they might also be expected to be exposed randomly to the satellite-derived space debris flux. For the small particulates, LDEF's offset of 8° to 9° increases the observed excess of the south flux relative to the North if true orbit pointing directions are considered. For larger particulates - shown to be predominantly interplanetary in origin (McDonnell, 1991), this offset correspondingly reduces the excess of the North relative to South for the penetrating flux at $f_{max} > 20$ microns but it remains significant. Explanations of this North-South asymmetry and its reversal within the MAP sensitivity regime call for a non-random spatial distribution of dust in Earth orbit, if the fluxes are dominated by "orbitals". Alternatively, if they are interplanetary a non-random distribution in interplanetary space is called for. Though precession generally randomizes the satellite population regarding the ascending nodes and argument of perigee, the geocentric inclination is retained except for the very smallest particles which can be influenced by the Lorentz force due to electromagnetic coupling of their electrostatic charge and the Earth's magnetic field. For one particular type of orbit - Molniya - an inclination of some 70° locks the precession into a stable geocentric relationship from which asymmetry *could* result. The IDE experiment (Mulholland et al, 1991) sheds significant light on the non-random time variations of what, on the MAP experiment, we see as a total 5.78 year accumulation.

Though LDEF offers unprecedented definition of the 1984-1990 flux, we should compare this to other data. We take, as one example, the SMM data, but not in terms of inferred impacting mass. The crater diameter D_C is referenced to an expected crater depth by the ratio observed for LDEF clamps (Newman, 1991) giving $P_c/D_C = .58$. We also use $f_{max} = 1.15\ P_c$ (McDonnell 1970), and combining these, $f_{max} = 1.15 \times .58\ D_C = .67\ D_C$. Alternatively we could choose $f_{max} = 1.7 \times .58\ D_C$ according to Humes (1990); this data from SMM is shown dotted line on Figure 8, and - if a random SMM exposure is simulated by

some averaging of the NSEW faces of LDEF MAP data - we see that the SMM data and LDEF MAP data are quite compatible.

2.3. Supra-Marginal Perforations.

Where $D_H > 0$ we have information which can sometimes lead to the clues on the particle size, mass or velocity. We cannot in general separate out these three parameters explicitly since in general the crater dimensions are a function of total particle *energy* at hypervelocities. For particle diameters $d_p > f_{max}$, however, we must see a trend towards a perforation comparable to the particle size. The velocity may also be inferred within broader limits from crater morphology. We summarise relevant penetration relationships used (Appendix) to transform the D_H distribution for one foil, the 5μm aluminium space-pointing foil, to an equivalent thickness of foil which would just be penetrated (Deshpande, 1991). Figure 9 shows this transformation; it is compared to the crater distribution on the space-pointing clamp analysed at Canterbury. Though this conversion is preliminary, and no doubt in need of refinement, we see some convergence. At large dimensions, statistical limits restrict the comparison, but the total LDEF data set will permit refinements of this transformation in due course.

2.4 Ultraheavy Cosmic-Ray Nuclei Experiment (UHCRE - AO178) Thermal Cover Penetration Data.

The $18m^2$ area of Fluorinated Ethylpropylene Teflon (FEP) thermal closeout covers show excellent promise for meteoroid and debris studies. Under agreement between the Principal Investigators (O'Sullivan et al, 1984), NASA LaRC and ESA, scanning operations were performed at NASA KSC after recovery and now continue at NASA JSC and the University of Kent at Canterbury, UK. These laminar foils comprise 120 microns of FEP Teflon, backed by a Silver/Inconel flash and some 80 microns of Chemglaze Z306 black paint. The equivalent thickness of aluminium penetrated may possibly be related using relationships in the Appendix. However this presumes we know the *dynamic* strengths involved; - the behaviour of the Teflon under impact is indeed complex and poses one of the more interesting morphological studies on LDEF. Figure 10 shows optical photographs of sample Teflon penetrations. They show (on the Silver surface beneath the Teflon) radial light and dark bands corresponding to variations in the Fluorine/Oxygen ratio. Though akin to "growth rings" it is uncertain whether they are formed completely at impact or involve a subsequent combination of delamination and the ingress of powerfully oxidizing atomic oxygen.

As a first sample of the UHCRE data we plot the hole size distribution on faces 10 and 4 from this experiment (Figure 11); corresponding approximately to an East-West configuration they yield small ratios e.g. 10 which demonstrates the need for a geocentric particle velocity much greater than LDEF's orbital velocity, namely from interplanetary hyperbolic sources. This is confirmed by the MAP data at $f_{max} = 30$ μm and the SDIE data (Humes, 1991).

2.5 Other LDEF data.

We piece together in Figure 12, albeit in tentative fashion, other data comprising that of the Interplanetary Dust Experiment (IDE - AO201, Mulholland, 1991); LDEF MAP (ibid), the Canterbury scanning of the UHCRE covers (O'Sullivan et al, 1984) and data from LDEF Meteoroid and Debris Special Interest Group (M+DSIG) data (See et al, 1990) including the preliminary scanning of the surfaces of the Humes Space Debris Impact Experiment (SDIE - S0001) performed at KSC after retrieval. We show also the data from the (West-pointing) French Co-operative Payload (Frecopa) tray (Mandeville, 1990). Data models for the West and East fluxes (representing approximately minimum (interplanetary) and maximum (interplanetary and earth-orbital)) have been developed (e.g Sullivan & McDonnell (1991)). This is used (Section 3) in the reduction of the data to a geocentric (compared to LDEF's orbital) reference frame. The first step requires comparison of the West and Space fluxes which are both predominantly interplanetary.

We shall later see this larger body of data refined in terms of resolution and accuracy but also in terms of the *calibration* i.e. the equivalence of different types of detector such as the IDE solid state SiO_2 detectors, the thicker targets of the Teflon UHCRE targets and the aluminium SDIE surfaces. Not all detectors have a common pointing direction, although we shall see that the IDE, MAP, UHCRE and SDIE experiments offer the fullest of angular coverage.

We also show data from the M+D SIG database, representing the LDEF tray clamp and frame impact crater counts on either 12 (x30°) or 24 (x15°) peripheral pointing directions (Figure 13) (See et al., 1990). The bias (for these larger particulates) towards geocentric North is seen. Accepting the discussions in Section 5 which support the interplanetary origin of these particulates, we see this argues for more of the large interplanetary particulates to be in the descending mode at 1 AU heliocentric distance. This has implications for the number of sources responsible for the sporadic micrometeoroid flux at some 50 μm particle diameter, a size which corresponds to particles responsible for the Zodiacal Light (e.g. Giese et al, 1976). These particulates were found assuming the single velocity (average) model, to have a geocentric velocity in the region of 17.4 ± 3 km sec^{-1}, transforming to a V_∞ of 12 ± 4 km sec^{-1} as the geocentric inferred average approach velocity to the Earth in our initial modelling (McDonnell, 1991) This is comparable to values derived from meteoroid studies e.g. see Zook 1975 for review. It is interesting to note that in similar modelling by Zook (1990), quantitative differences are obtained. For given Space-to-West and East-to-West ratios, Zook's modelling calls for geocentric velocities higher by some 5 km s^{-1} than ours leading to interplanetary approach velocities of some 19 kms^{-1}. *Both* modelling approaches however demonstrate the extraterrestrial (and interplanetary) nature of the large particles.

The transformation of Sullivan & McDonnell (1991) is further applied to the West flux to predict the East, using a data model developed from Figure 12. This yields a flux lower, by a factor of 4, than the measured East flux, and calls for the presence of Earth-orbitals; the transformation and discussion is described in McDonnell (1991) and results shown in Figure 14.

3. MODELLING OF LDEF'S EXPOSURE IN THE PARTICULATE ENVIRONMENT.

In all modelling of the dynamics of particle orbits and interception with a moving spacecraft, the examination and interpretation of impact/flux data from differing spacecraft attitudes or pointing directions must be conducted either at *constant mass* or alternatively at *constant crater size*. Crater size is, of course, directly related to the marginal perforation foil thickness.

Flux enhancement at constant mass is the "sweeping-up" effect of the satellite into the particulate cloud and leads to an enhancement of numbers intercepted compared to the trailing face. A consequential effect of this, but quite separate physically, is that those particles will also have a different relative velocity for the two faces, and hence, will upon impact lead to different crater dimensions; because most impact observations (and observed crater flux distributions) refer to a particular crater *dimension*, the experiment detector surfaces receiving greater numbers of particles will yield a flux value which is relevant to smaller (and invariably more numerous) particles. The latter *sensitivity enhancement* depends on the size distribution of particulates which, fortunately, can be deduced from the data.

The approach to this dynamic *modelling* is described by McDonnell et al (1990), and uses a geocentric distribution of particle directions at a particular velocity; when combined with LDEF's motion the incidence frequency (flux) on LDEF's faces and also the impact velocity is calculated. The normal velocity (which determines the effective velocity for impact penetration) is calculated. The results are applied first to the West and Space flux, which cannot intercept significant orbital particulates. The transformation is effected as a function of velocity and a particle velocity is found which leads to best agreement between the West and Space flux data.

We see in Figure 14 the resultant Earth-orbital component identified, which dominates the East, and also the North and South fluxes for $f_{max} < 20$ μm. This is in contrast to the larger particulates where the interplanetary component is dominant. We can also transform (McDonnell, 1991) to the expected interplanetary flux at 1AU beyond the gravitational influence of the Earth. This compares very favourably with deep space data and meteoroid fluxes (as reviewed by Grün et al 1985), confirming our hypothesis of the dominant sources of the LDEF impacts.

As to the astrophysical or terrestrial *origin* of the Earth orbitals, from consideration of the IDE flux and temporal variations, Mulholland et al (1991) have claimed they are space debris related. A contrary viewpoint has been proposed by McDonnell (1991) and McDonnell & Ratcliff (1991) where the possibility of captured interplanetary dust either through *aerocapture*, and *aero-fragmentation* capture is discussed. The

electrostatic disruption of fragile meteoroids near the earth has been proposed as a means of explaining the groups and swarms of particulates seen by Heos II (Hoffman et al., 1975(b)).

We probably must await chemical evidence before the *true* origin is ascertained. Although the SMM data had previously been attributed to space debris and calculated to be some 50 times higher in flux than the natural component, we see that improved penetration formula lead to the excess being much less because of the lower inferred mass of these particulates (even though they might comprise space debris). That data did show their chemistry to be debris-related, but the equivalence of LDEF MAP and SMM flux data, separated by some 5 years in epoch shows little evidence of a change of flux in a period when activity might have expected to increase. We shall have to "watch this space" for further developments!

ACKNOWLEDGEMENTS

To the Science and Engineering Research Council UK for financial support and Auburn University Space Power Institute (USA), N660921-86-OC-A226, subcontract 87-212. To the whole LDEF MAP team; Ken Sullivan, Piers Newman, Sunil Despande, Matthew Paley particularly. To the USS secretarial complement, Alison and Margaret, and to NASA Langley Project Office especially Jim Jones and Bill Kinard for every encouragement throughout the project.

APPENDIX

Penetration Relationships Used

For thin (micron dimension) aluminium foils impacted by iron particles, we refer to calibration data established to velocities of 15 km s^{-1} using a 2 MV van der Graaff accelerator (McDonnell, 1970). This yields a marginal penetration relationship:

$$f_{max} = 0.79\ V^{0.763} \qquad \text{(eq 1)}$$

where V is the impact velocity (km s^{-1}) and f_{max} (μm) is the foil thickness penetrated, not referred to the *ballistic limit*, but to a value of $D_H = f_{max}$. In practice, the minimum hole size close to the ballistic limit yields a value of $D_H/f_{max} = 0.6$ for iron particles impacting aluminium at velocities of some 5 km s^{-1} due to the formation of deeper craters. At higher velocities, the ballistic limit perforation leads to a minimum hole size which is typically $D_H \approx f_{max}$, although in principle a hole of $D_H = 0$ is (on the limit) still technically feasible.

The above formula was extended to cover the region beyond the ballistic limit (Carey et al. 1985) for iron projectiles impacting on aluminium targets namely:

$$\frac{D_H}{d_P} = 1 + 1.5\,(f/d_P)\,V^{0.3}\left[\frac{1}{1 + (f/d_P)^2\,V^{-n}}\right] \qquad \text{(eq 2)}$$

where V is in kms^{-1} and n is given by,

$$n = 1.02 - 4\exp(-0.9\,V^{0.9}) - 0.003\,(20 - V) \qquad \text{(eq 3)}$$

A formula derived from iron projectiles impacting on gold targets (and hence comparable to low density meteoroids impacting aluminium, because of the similar projectile-to-target density ratios) was also derived in the same work:

$$\frac{D_H}{d_P} = 1 + 5\,(f/d_P)\,V^{0.3}\left[\frac{1}{1 + 7\,(f/d_P)^2\,V^{-n}}\right] \qquad \text{(eq 4)}$$

The value of n is as above.

These formulae are solved to yield the diameter of impacting particle d_P from a given value of D_H and velocity V. The marginal penetration distance is then calculated from d_P and V to yield an equivalent value of f_{max}. This transformation (illustrated in Figure 9) is relatively insensitive to the velocity assumed.

Neither of these relationships include dimensional scaling, and the first relationship (eq 1) applies only to iron projectiles on aluminium. The ballistic limit formula has therefore been generalised by McDonnell & Sullivan (1991) to yield a relationship applicable to foils over a wider range of dimensions and for various projectile-target densities and strengths:

$$\frac{f}{d_P} = 1.023\,d_P^{0.056}\left(\frac{\rho_P}{\rho_T}\right)^{0.476}\left(\frac{\sigma_{Al}}{\sigma_T}\right)^{0.134} V^{0.664} \qquad \text{(eq 5)}$$

Here, f and d_P are in units of cm, the densities, ρ, are in g cm^{-3}, the velocity in km s^{-1} and the target tensile strength, σ_T, in units of MPa. It is to be noted that this contrasts with the dimensional dependence of the ballistic limit formula of Pailer and Grün (1985) where a very strong dimensional dependence of the form $d_P^{0.21}$ is demonstrated compared to a dimensional dependence of the form $d_P^{0.056}$ in ours and other work. The formula of Pailer & Grün (1985) yields

$$\frac{f}{d_P} = 0.772\,d_P^{0.2}\,\varepsilon^{-0.06}\,\rho_P^{0.73}\,\rho_T^{-0.5}\,(V\cos\alpha)^{0.88} \qquad \text{(eq 6)}$$

where ε is the target foil ductility and α is the angle of impact relative to the normal.

This formula (eq 6) however, has been shown to be unsuitable to interpret the SMM data (McDonnell, 1991) and previously led to an overestimate of the flux of space micro-debris relative to the natural environment (Lawrence & Brownlee, 1985).

Reference may also be made to other formula commonly used, namely that of Fish and Summers (1965):

$$\frac{f}{d_P} = 0.57\,d_P^{0.056}\,\varepsilon^{-0.056}\left(\frac{\rho_P}{\rho_T}\right)^{0.5} V^{0.875} \qquad \text{(eq 7)}$$

Nauman (1966) developed the relationship:

$$\frac{f}{d_P} = d_P^{0.056}\,\rho_P^{0.52}\,V^{0.875} \qquad \text{(eq 8)}$$

and Cour-Palais (1969) used a similar equation, namely:

$$\frac{f}{d_P} = 0.635\, d_P^{0.056}\, \rho_P^{0.5}\, V^{0.67} \qquad \text{(eq 9)}$$

All formulae have been converted to the same units as in equation 5. The McDonnell-Sullivan equation concurs with the more accepted of these relationships at centimetre scale but also has the benefit of fitting the microscale regime. LDEF's impact record may enable some of these parametric dependencies to be tested at the more realistic velocities occurring during its 5.75 year exposure.

REFERENCES

Carey, W.C., McDonnell, J.A.M. and Dixon, D.G., (1985) "An Empirical Penetration Equation for Thin Metallic Films used in Capture Cell Techniques", In Properties and Interactions of Interplanetary Dust, D. Reidel, R.H., Giese and Ph. Lamy (eds.), pp. 131-136.

Cour-Palais, B.G., (1969) "Meteoroid Environment Model -1919", NASA SP-8013.

Deshpande, S.P. and Paley, M.T., (1991) "Supra-Marginal Impacts Detected on the Microabrasion Package (MAP) Experiment Situated on LDEF's Space Face", Proc. Workshop on Hypervelocity Impacts in Space, University of Kent at Canterbury, Dec. 1991.

Fechtig, H., (1976) "In-situ records of interplanetary dust particles - methods and results", Proc. IAU Colloq. 31, Lecture Notes in Physics, **48**, p 143, Eds. H. Elsasser & H. Fechtig, Springer-Verlag.

Fish, J.L. & Summers, J.L. (1965) Proc. Hypervelocity Impact Symposium, 7th, **3**, 2.

Giese, R.H. and Grün E., (1976) "The Compatibility of Recent Micrometeoroid Flux Curves with Observations and Models of the Zodiacal Light", Lect. Notes Phys. **48,** pp. 135-139.

Grün E., Zook, H.A., Fechtig, H. and Giese, R.H., (1985) "Collisional Balance of the Meteoritic Complex", Icarus **62,** pp. 244-272.

Hoffmann, H.J., Fechtig, H., Grün, E. and Kissel, J., (1975(a)) " First Results of the Micrometeoroid Experiment S215 on HEOS 2 Satellite", Planet. Space Sci. **23,** pp. 215-244.

Hoffmann, H.J., Fechtig, H., Grün, E. and Kissel, J., (1975(b)) "Temporal Fluctuations on anisotropy in the Earth Moon System", Planet. Space Science, **23**, pp. 985-991.

Hörz, F., See, T.H. and Bernhard, R., (1991) "Thin Film Penetrations by 50 to 3200 μM Diameter Glass Projectiles", Proc. Workshop on Hypervelocity Impacts in Space, University of Kent at Canterbury, Dec. 1991.

Humes, D.H., (1991) "The SDIE Impact Experiment on LDEF", Proc. Workshop on Hypervelocity Impacts in Space, University of Kent at Canterbury, Dec. 1991.

Laurance, M.R. and Brownlee, D.E., (1986) "The Flux of Meteoroids and Orbital Space Debris Striking Satellites in Low Earth Orbit", Nature, **323,** pp. 136-138.

Mandeville, J.C. and Berthoud L., (1991) "Hypervelocity Impacts on Space Retrieved Surfaces (LDEF and MIR)", Proc. Workshop on Hypervelocity Impacts in Space, University of Kent at Canterbury, Dec. 1991.

McDonnell J.A.M., Carey, W.C. and Dixon, D.G., (1984) "Cosmic Dust Collection by the Capture Cell Techniques on the Space Shuttle", Nature, Vol. **309**, No. 5965, pp. 237-240.

McDonnell, J.A.M., (1970) "Factors Affecting the Choice of Foils for Penetration Experiments in Space", COSPAR Space Sci. Sym., Prague, 1969, Space Research **X,** pp. 314-325.

McDonnell, J.A.M., (1970) "Review of In-Situ Measurements of Cosmic Dust Particles in Space", XIIIth COSPAR Space Sci. Sym., Leningrad, Space Research XI-Akademie-Verlag (Berlin), pp 415-435.

McDonnell, J.A.M., (1978) "Microparticle Studies by Space Instrumentation", In Cosmic Dust , Chapter 6, pp. 337-419. Editor J.A.M. McDonnell, Publishers John Wiley and Sons.

McDonnell, J.A.M., (1991) " Impact Cratering from LDEF's 5.75 year Exposure: Decoding of the Interplanetary and Earth-Orbital Populations", Proc. 22nd Lunar & Planetary Science Conference, Houston.

McDonnell, J.A.M., Deshpande, S.P., Green, S.F., Newman, P.J., Paley, M.T., Ratcliff, P.R., Stevenson, T.J. and Sullivan, K., (1990) "First Results of Particulates Impacts and Foil Perforations on LDEF", Adv. Space Res. Vol. II, No. 12, [12]109–[12]114, 1991.

Mulholland, J.D., Oliver, J.P., Singer, S.F., Weinberg, J.L., Cooke, W.J., Montague, N.L., Kassel, P.C., Wortman, J.J., Kinard, W.H. and Simon, C.G., (1991) "LDEF Interplanetary Dust Experiment: A high Time-Resolution Snapshot of the Near-Earth Particulate Environment", Proc. Workshop on Hypervelocity Impacts in Space, University of Kent at Canterbury, Dec. 1991.

Naumann, R.J., (1966) "The Near Earth Meteoroid Environment", NASA TN D-3717.

Newman, P.J., (1991) "A Comparison of the Micrometeoroid Environment as Measured by Thick and Thin Targets from the East Face of the Long Duration Exposure Facility", Proc. Workshop on Hypervelocity Impacts in Space, University of Kent at Canterbury, Dec. 1991.

O'Sullivan, D., Thompson, A., Ceallaigh, C., Domingo, V. and Wenzel, K.P. (1984) "The Long Duration Exposure Facility (LDEF) Mission 1 Experiments, A High Resolution Study of Ultra-Heavy Cosmic-Ray Nuclei (AO178)", NASA SP-473.

Pailer, N. and Grün, E., (1980) "The Penetration Limit of Thin Films", Planetary and Space Science **28,** pp. 321-331.

Paley, M.T., (1991) "An Automated System for Obtaining Impact Penetration, Location, Size and Circularity, on a Foil with Special Reference to LDEF," Proc. Workshop on Hypervelocity Impacts in Space, University of Kent at Canterbury, Dec. 1991.

See, T., Allbrooks, M., Atkinson, D. Simon, C. and Zolensky, M., (1990) "Meteoroid and Debris Impact Features Documented on the Long Duration Exposure Facility, NASA JSC Planetary Materials Branch Publication #84, August 1990.

Sullivan, K., and McDonnell, J.A.M., (1991) "LDEF Flux Anisotropy: Dynamic Modelling and Flux Transformations to Define the Interplanetary Micrometeoroid Environment", Proc. Workshop on Hypervelocity Impacts in Space, University of Kent at Canterbury, Dec. 1991.

Zook, H.A., (1975) "The State of Meteoritic Material on the Moon" Proc. Lunar Sci. Conf. 6th, pp. 1653-1672.

Zook, H.A., (1991) "Meteoroid Directionality on LDEF and Asteroidal versus Cometary Sources", Abstract, Proc. Lunar Planet Sci Conf. 22nd, pp 1577-1578.

Year	Altitude H (km)	H+R_E (km)	Fraction of year	Horizon angle (deg)	Effective flat plate solid angle (ster)
1984	478	6849	0.745	106.82	2.141
1985	473	6844	1.000	106.68	2.137
1986	470	6841	1.000	106.60	2.136
1987	468	6839	1.000	106.54	2.134
1988	459	6830	1.000	106.28	2.124
1989	410	6781	1.000	104.80	2.077
1990	340	6711	0.033	102.34	1.995

Table 1. Exposure Factors of MAP aboard LDEF, giving yearly mean altitudes and Earth shielding history.

Face	Nominal Thickness (μm)	Measured Thickness (μm)	# holes	Area (m^2)	Flux ($m^{-2}s^{-1}$)
East	5	4.83	435	1.02×10^{-2}	2.35×10^{-4}
MAP	12	12.13	49	2.67×10^{-3}	1.01×10^{-4}
	14	14.11	73	5.21×10^{-3}	7.69×10^{-5}
	18	18.16	104	1.02×10^{-2}	5.61×10^{-5}
	25	24.13	40	7.89×10^{-3}	2.79×10^{-5}
	30	31.14	21	1.02×10^{-2}	1.13×10^{-5}
West	3	3.1	(22)	5.33×10^{-3}	2.27×10^{-5}
MAP	2.5	3.72	(6)	5.33×10^{-3}	6.19 x 10-6
	5	4.83	26	2.03×10^{-2}	7.02 x 10-6
	12	12.13	1	2.67×10^{-3}	2.06 x 10-6
	14	14.11	2	5.21×10^{-3}	2.11 x 10-6
	18	18.16	5	1.02×10^{-2}	2.70 x 10-6
	25	24.13	11	1.81×10^{-2}	3.35 x 10-6
	30	31.14	3	2.03×10^{-2}	8.10 x 10-7
North	1.5	2.02	(361)	5.33×10^{-3}	3.72×10^{-4}
MAP	2.5	3.72	(298)	1.07×10^{-2}	1.54×10^{-4}
	5	4.83	467	2.03×10^{-2}	1.26×10^{-4}
	12	12.13	22	5.80×10^{-3}	2.08×10^{-5}
	14	14.11	26	5.21×10^{-3}	2.74×10^{-5}
	18	18.16	41	1.02×10^{-2}	2.21×10^{-5}
	25	24.13	38	2.04×10^{-2}	1.03×10^{-5}
	30	31.14	43	2.03×10^{-2}	1.16×10^{-5}
South	1.5	2.02	(1158)	1.07×10^{-2}	5.97×10^{-4}
MAP	3	3.1	(218)	5.33×10^{-3}	2.25×10^{-4}
	2.5	3.72	(187)	5.33×10^{-3}	1.93×10^{-4}
	5	4.83	570	2.03×10^{-2}	1.54×10^{-4}
	12	12.13	28	2.67×10^{-3}	5.75×10^{-5}
	14	14.11	45	5.21×10^{-3}	4.74×10^{-5}
	18	18.16	61	1.02×10^{-2}	3.29×10^{-5}
	25	24.13	23	1.81×10^{-2}	7.00×10^{-6}
	30	31.14	13	2.03×10^{-2}	3.51×10^{-6}
Space MAP	5	4.83	193	3.10×10^{-2}	3.42×10^{-5}

Table 2. Characteristic areas and detected numbers of perforations of the MAP deployment on LDEF. Only the surfaces scanned to date are shown; for foils of less than 5 microns, penetrations (in parentheses) are tentative. For foils of 5 microns or greater. 2,340 perforations are reported.

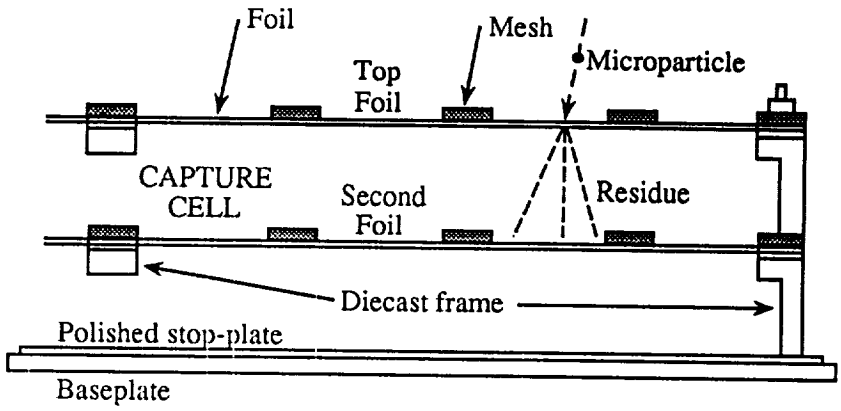

Fig. 1. Schematic cross-section of Microabrasion Package (MAP) Experiment configuration. The capture cell system is formed between the top and second foil surfaces. By inversion of the frame orientation differing foil spacings are achieved.

Fig. 2. Plan view of MAP package giving effective foil areas and the distribution of perforations determined by post-flight optical scanning.

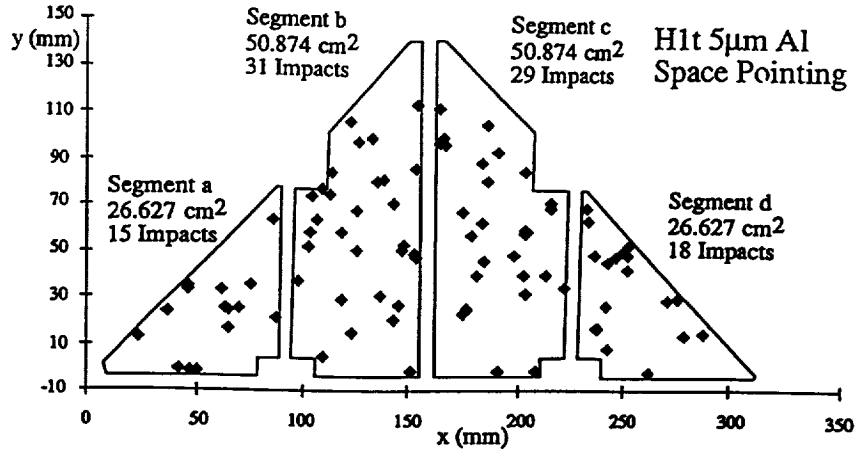

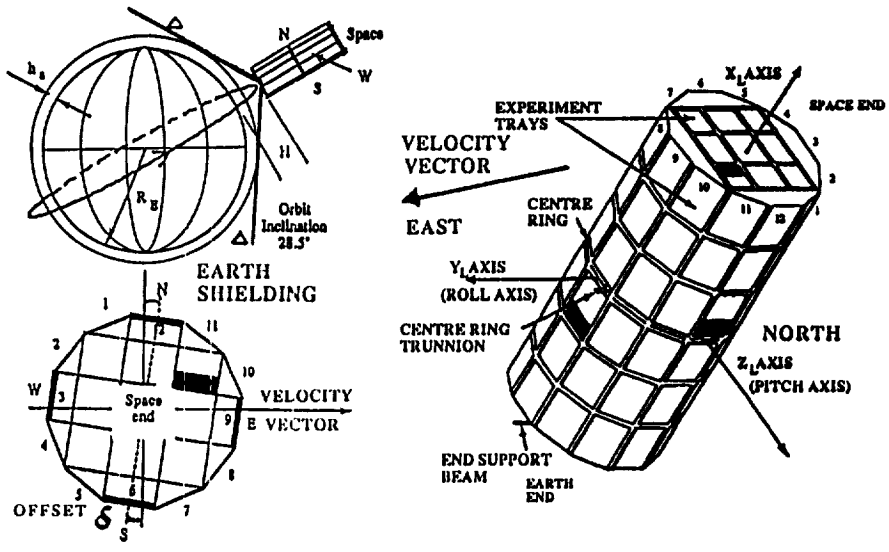

Fig. 3. MAP locations (shaded) on LDEF and the offset of deployment δ illustrated relative to the motion vector (8° to 9°). The Earth shielding angle Δ is illustrated (left).

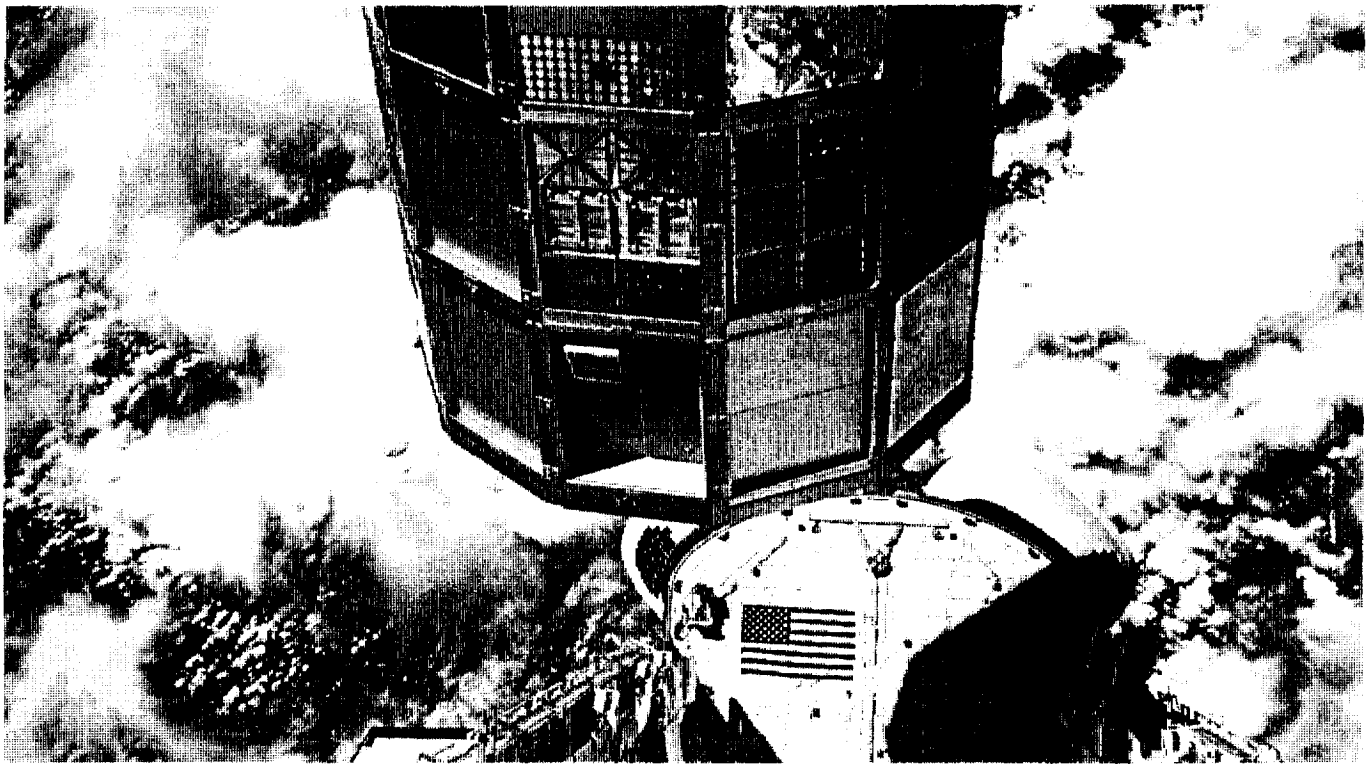

Fig. 4. Peripheral experiment locations photographed at LDEF retrieval. The MAP experiment (top of second tray up, left of centre) is one of the five such locations. NASA Photo.

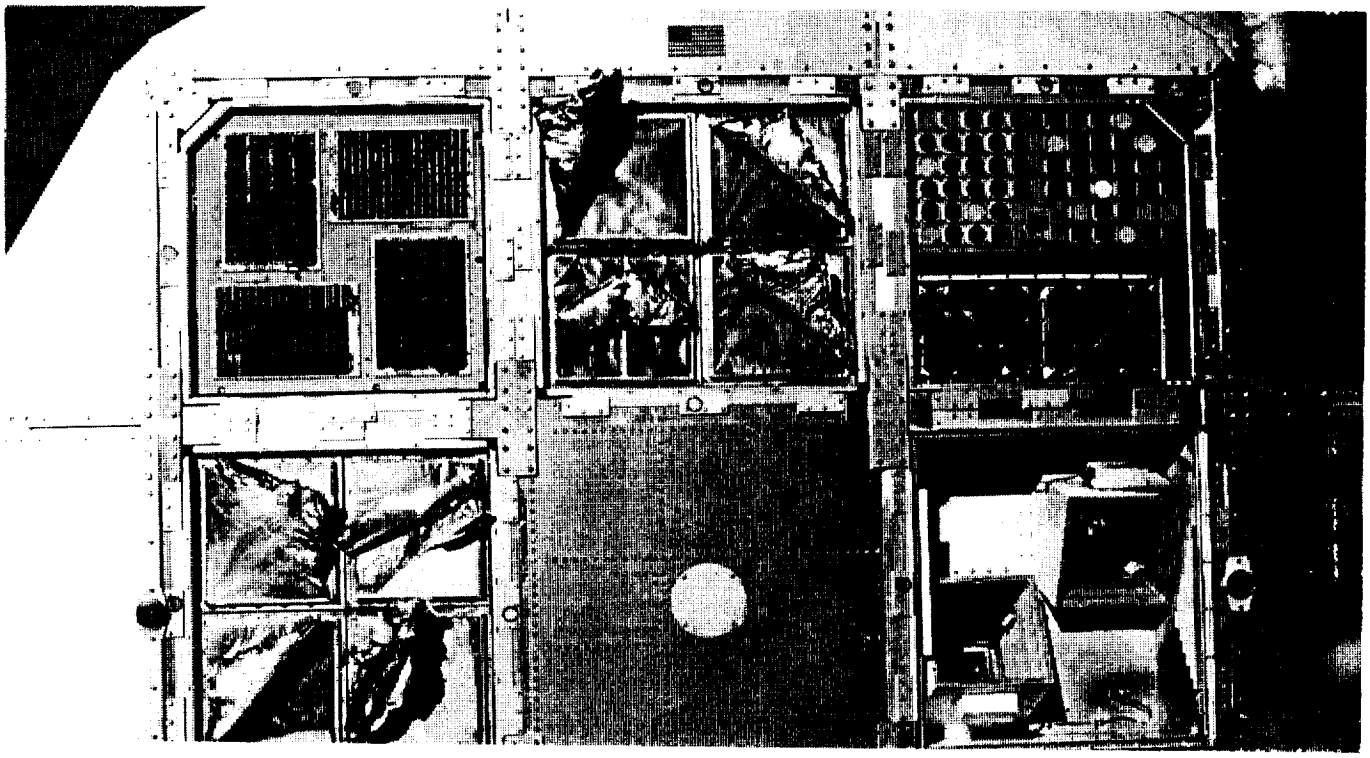

Fig. 5. Space-facing MAP location at LDEF retrieval. The micron dimensioned foils (upper right tray, lower half) show excellent integrity despite a thermal cycling, totalling some 35,000. By contrast, the coated Mylar capture cell covers of the other impact experiments and the multilayer insulation of the NRL cosmic ray experiment (shown in this photograph) suffered considerable degradation. NASA Photo .

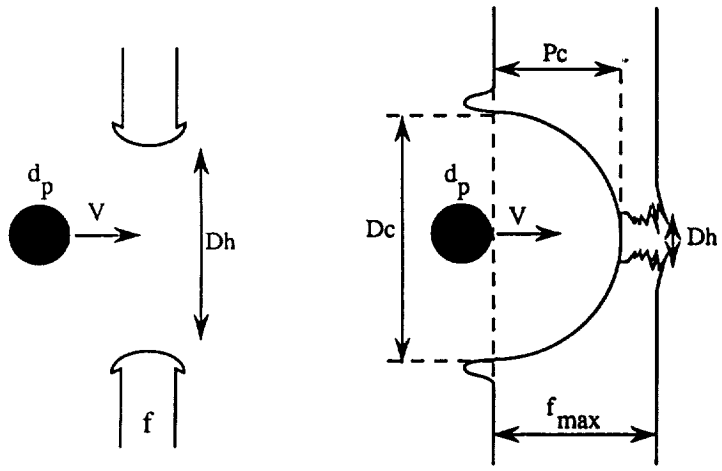

SUPRA-MARGINAL

MARGINAL (AT BALLISTIC LIMIT)

Fig. 6. Parameters of hypervelocity impact craters measured for non-penetrating impacts in (a) the penetration of foils and a semi-infinite target (b) . Where $D_H > f_{max}$ the opportunity to capture material on the second surface exists. The maximum thickness a foil perforated f_{max} is related to the semi-infinite target penetration by the relationship $f_{max} = KP_c$. K = 1.15 has been reported for iron particles impacting on aluminium (McDonnell, 1970) and alternatively K = 1.5 to 1.7 (Humes, 1991) reported based on LDEF studies.

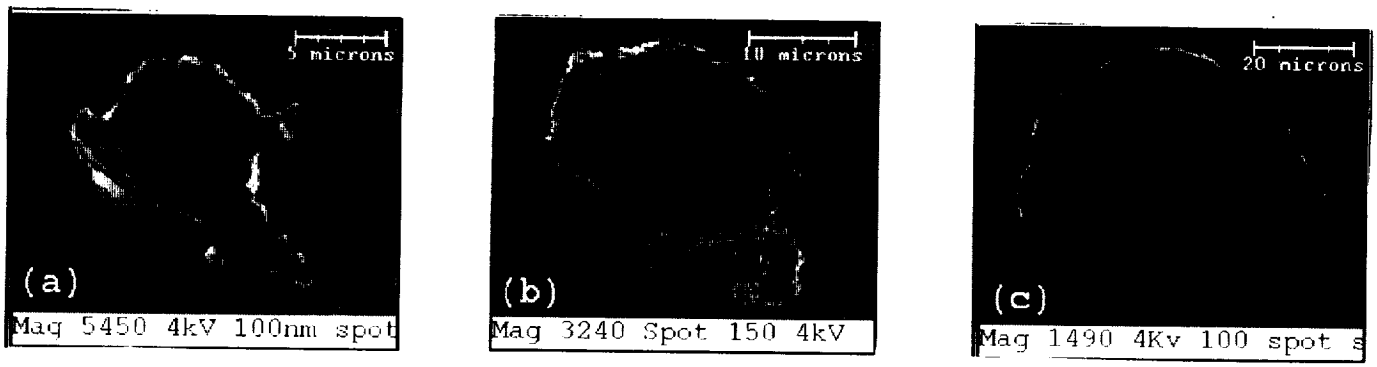

Fig. 7. Perforations in the MAP aluminium foils showing various morphologies dependent largely on the particle size and velocity relative to foil thickness. (a) shows the exit side just above the ballistic limit (b) the exit side for a large impact. In (c) a very large particle, perhaps 30 microns diameter, leads to a 60 micron diameter perforation and a clear signature for capture cell analysis.

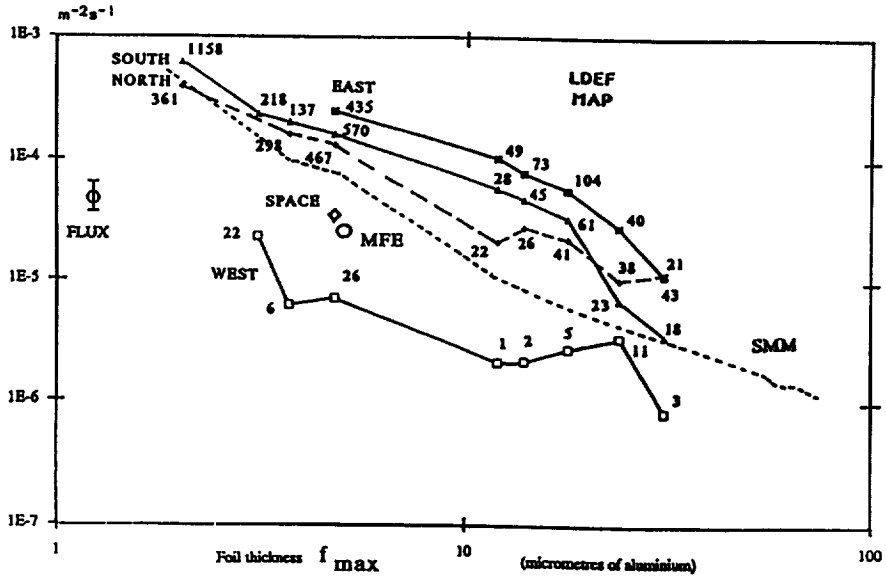

Fig. 8. MAP cumulative penetration distributions for 5 pointing directions showing the number of particles detected. Statistical errors are largely insignificant except for e.g. the low flux West directions. The North-south asymmetry is significant as indeed its reversal between large and small particulates.

Q-6

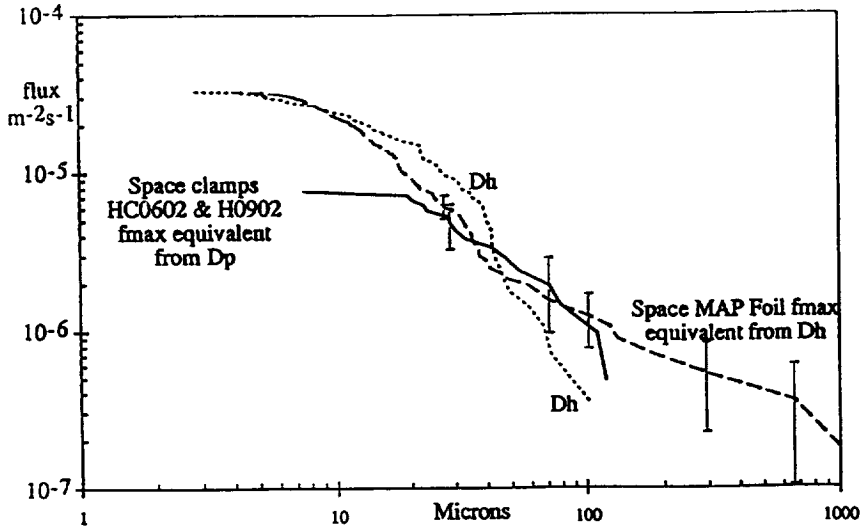

Fig. 9. MAP data from Space-pointing 5 micron foil plotted as a function of the hole diameter distribution D_H (dotted line). It is then transformed using a penetration relationship (Carey et al. 1985) to an equivalent foil penetration distribution (dashed line) and compared to LDEF clamp crater data also transformed to an equivalent foil penetration distribution (solid line).

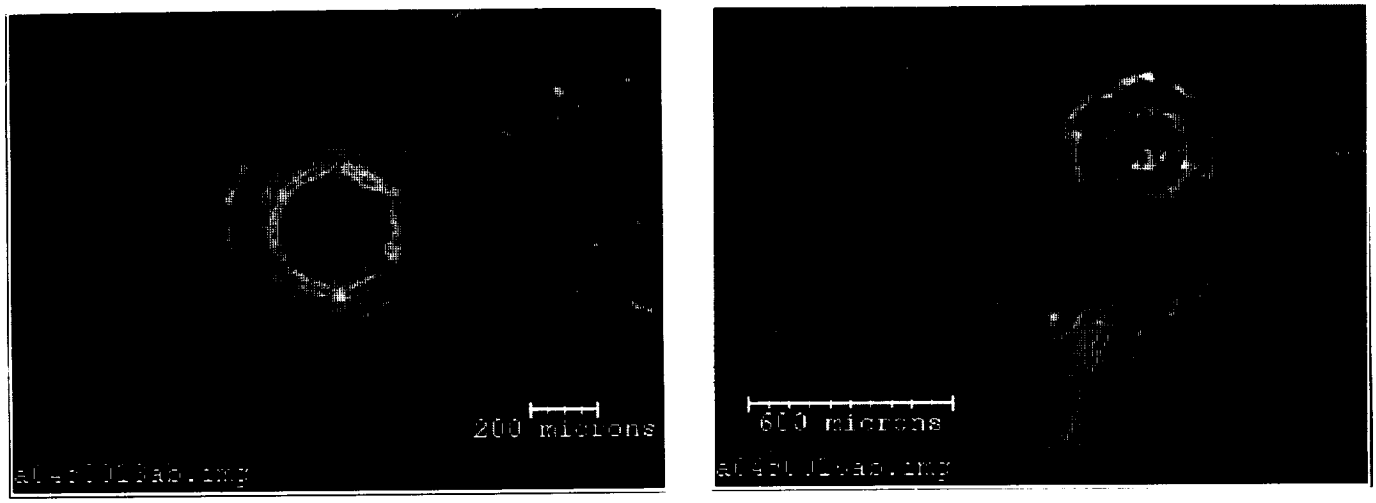

Fig. 10. Impacts of the FEP UHCRE Teflon covers showing (a) central pit . and (b) an extended spallation zone with radial cracks and circular features.

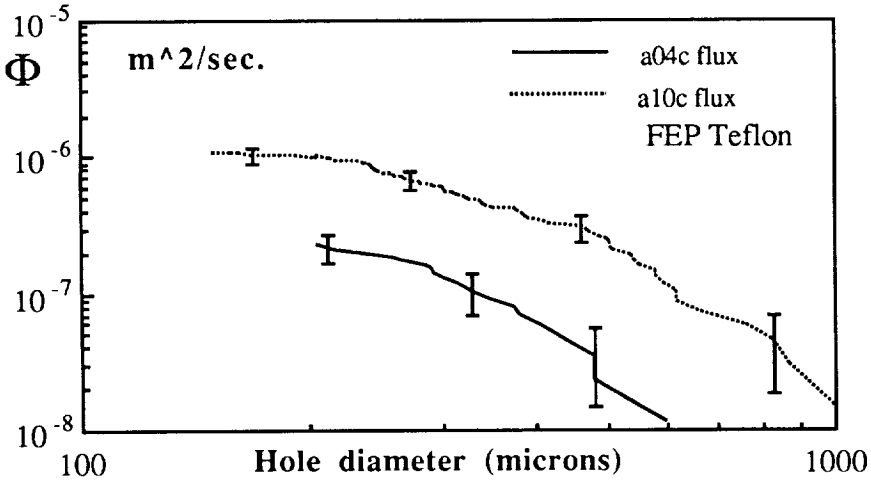

Fig. 11. Perforation hole distributions for a near East (Row 10) and near West (Row 4) FEP UHCRE Teflon surface. The flux ratio calls for particle velocities characteristic of interplanetary sources which are hyperbolic at LDEF's orbit. Particle velocities correspond to 17.4 ± 3 kms^{-1} in geocentric space and a V. of some 12 kms^{-1} on approach to the Earth.

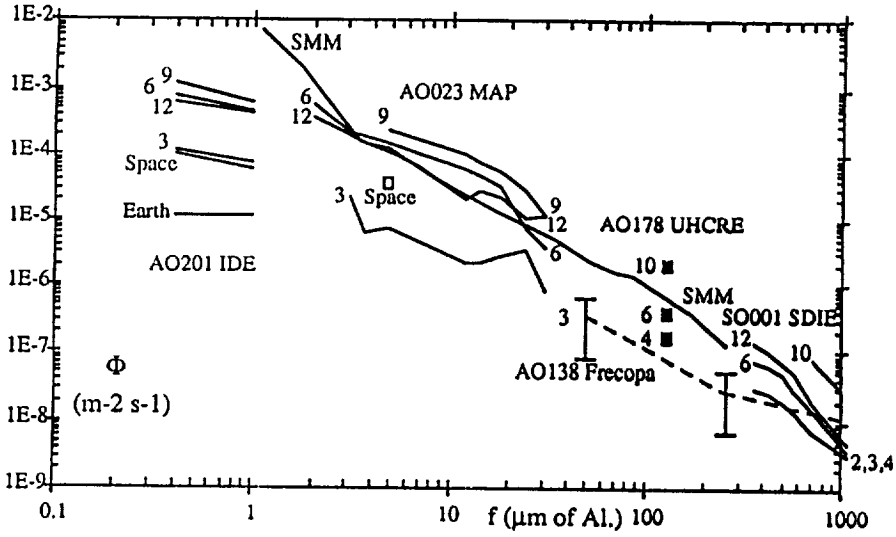

Fig. 12. Data from MAP foils set in the wider context of other LDEF data referenced to an equivalent penetration thickness of aluminium. A data model is derived for the East and West fluxes (section 3.1).

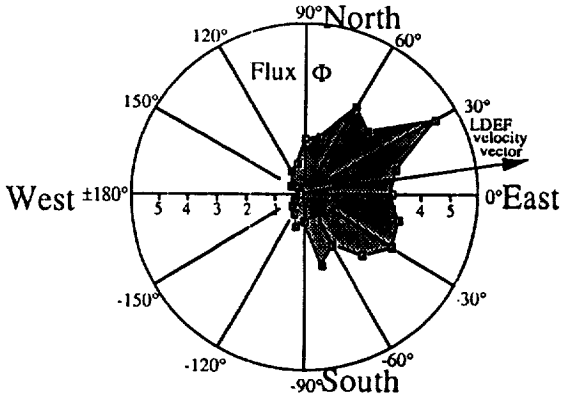

Fig.13 Angular dependence of the flux Φ (x10^7m-2s-1) for larger craters Dc>500μm for the Meteoroid and Debris Special Interest Group (M+D SIG) data base. A clear departure from symmetry is seen with a bias towards North, as distinct from the South bias at smaller dimensions seen on the MAP thin foils (<20μm).

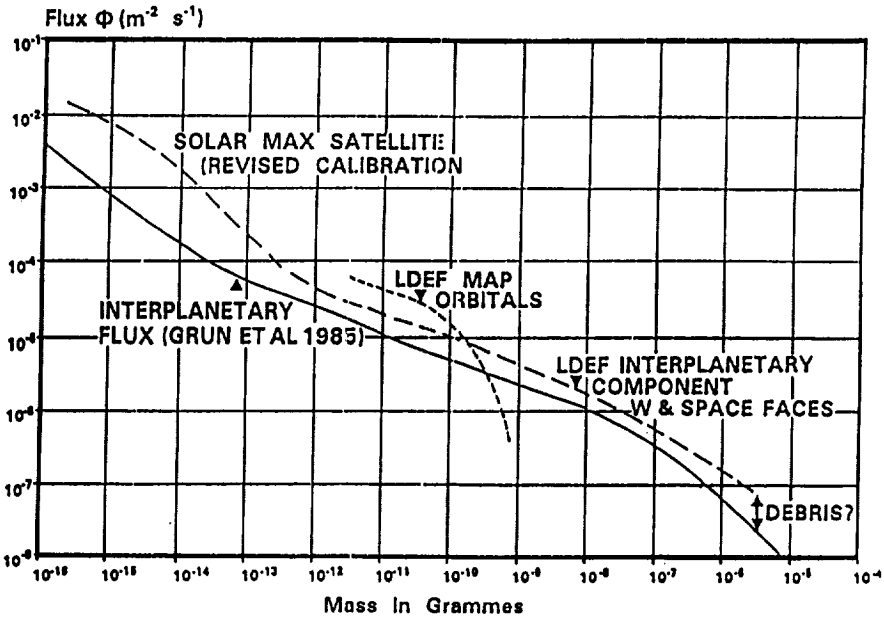

Fig. 14. Characteristics of the near Earth space particulate environment. Modelling involving a transformation between the West and Space (interplanetary dominated fluxes) yielding a geocentric particle velocity of 17.4 ± 3 kms^{-1}. The same particulates cannot fully account for the observed East fluxes and demonstrate (supported by the Space-to-North and Space-to-South fluxes) the presence of an Earth orbital component labelled MAP orbitals. Agreement between the LDEF space and West flux data transformed to interplanetary space at 1 AU (using Earth shielding and gravitational enhancement factors) is seen to be good.